Check for updates

ARTICLE   **OPEN**

E-cigarette and food flavoring diacetyl alters airway cell morphology, inflammatory and antiviral response, and susceptibility to SARS-CoV-2

Stephanie N. Langel [1,7], Francine L. Kelly[2,7], David M. Brass[2], Andrew E. Nagler[2], Dylan Carmack[2], Joshua J. Tu [3,4], Tatianna Travieso[3,5], Ria Goswami[6], Sallie R. Permar[6], Maria Blasi [3,5,7 ✉] and Scott M. Palmer[2,7]

Diacetyl (DA) is an α-diketone that is used to flavor microwave popcorn, coffee, and e-cigarettes. Occupational exposure to high levels of DA causes impaired lung function and obstructive airway disease. Additionally, lower levels of DA exposure dampen host defenses in vitro. Understanding DA's impact on lung epithelium is important for delineating exposure risk on lung health. In this study, we assessed the impact of DA on normal human bronchial epithelial cell (NHBEC) morphology, transcriptional profiles, and susceptibility to SARS-CoV-2 infection. Transcriptomic analysis demonstrated cilia dysregulation, an increase in hypoxia and sterile inflammation associated pathways, and decreased expression of interferon-stimulated genes after DA exposure. Additionally, DA exposure resulted in cilia loss and increased hyaluronan production. After SARS-CoV-2 infection, both genomic and subgenomic SARS-CoV-2 RNA were increased in DA vapor- compared to vehicle-exposed NHBECs. This work suggests that transcriptomic and physiologic changes induced by DA vapor exposure damage cilia and increase host susceptibility to SARS-CoV-2.

INTRODUCTION

Diacetyl (DA) is a volatile α-diketone used to impart a buttery-like aroma and flavor to a variety of food products and electronic cigarettes (e-cigs). Despite the widespread use of flavoring chemicals in e-cigs [1], very little is known regarding the negative impact of these chemicals on e-cig users. Although concerns regarding e-cig use and vaping primarily focus on nicotine and cannabis-derived compounds like tetrahydrocannabinol, DA is linked to a variety of toxic effects in the lung and airway cells. For example, DA exposure promotes oxidative stress, upregulates inflammatory processes including IL-8 secretion, cilia loss, and dedifferentiation of the epithelial layer in vitro [2–6]. This is relevant considering clinical and experimental evidence links the development of bronchiolitis obliterans ("popcorn lung") and irreversible lung disease to occupational DA exposure [7].

The significant proportion of e-cig use among youth combined with the demonstrated adverse effects of e-cig components like DA on airway epithelium, suggests e-cig use may be an important risk factor for coronavirus disease (COVID)-19, particularly in adolescents. Indeed, COVID-19 diagnosis was five times more likely among adolescent and young adult e-cig users as compared to non-users [8]. Previous evidence demonstrated that e-cig exposure significantly impaired antiviral host defenses and increased the influx of inflammatory neutrophils, potentiating immune-based pathology [9, 10]. Additionally, chronic e-cigarette vapor exposure has been shown to alter the physiology of lung epithelial cells and resident immune cells and to promote poor response to viral challenge in mice [11]. The broad range of pulmonary toxicity of e-cig components [12, 13], and the impact of flavoring agents such as DA on the airway epithelium inflammatory and antiviral responses, may predispose individuals to lung injury and severe COVID-19 following SARS-CoV-2 infection.

To evaluate the impact of multiple DA exposures on human airway epithelium, we assessed cellular morphology and transcriptional profiles of DA vapor-exposed normal human bronchial epithelial cells (NHBECs). Additionally, we determined if DA vapor exposure altered susceptibility to SARS-CoV-2 infection. This work provides new insights into early transcriptional responses and cilia loss to repeated DA vapor exposure that may contribute to the development of flavoring-induced airway disease and increased susceptibility to SARS-CoV-2 infection.
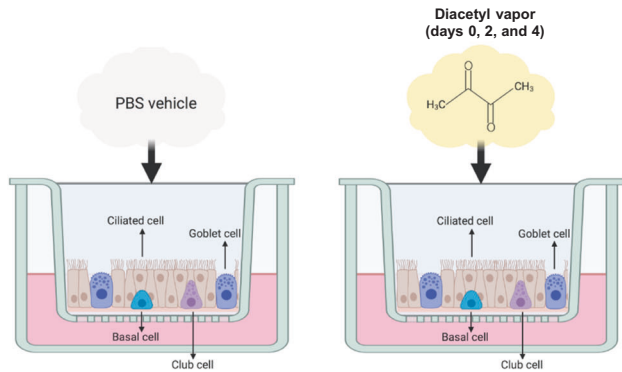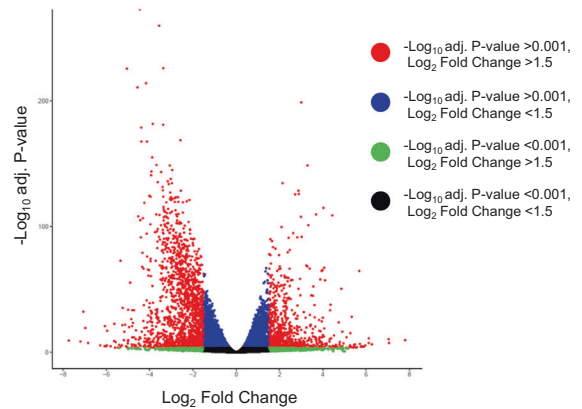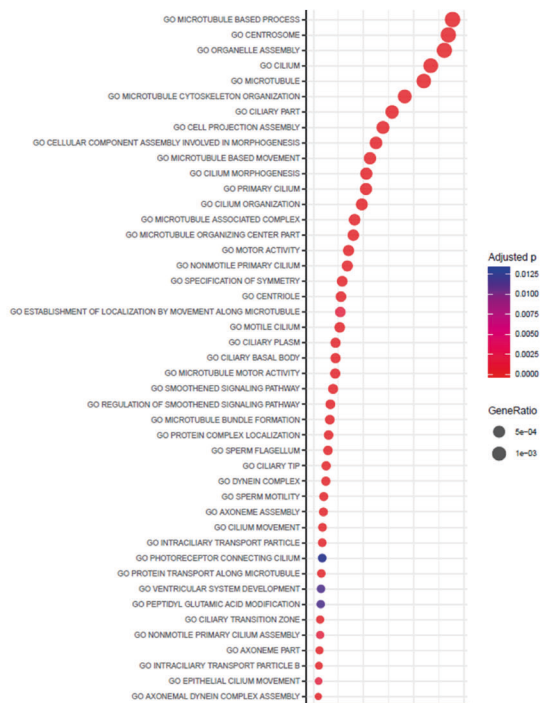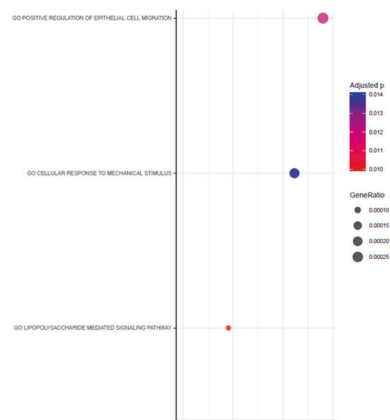
RESULTS

DA vapor exposure drives differential transcriptomic responses in NHBECs and reveals cilia injury signatures

NHBECs were exposed to PBS vehicle or DA vapor (Fig. 1A) for 1 h on days 0, 2, and 4 prior to RNA isolation and RNA-seq analysis on day 6. The hierarchical and principal component analyses and

[1]Duke Center for Human Systems Immunology and Department of Surgery, Durham, NC, USA. [2]Duke Clinical Research Institute and Department of Medicine, Duke University Medical Center, Durham, NC, USA. [3]Duke Human Vaccine Institute, Duke University Medical Center, Durham, NC, USA. [4]Department of Pediatrics, Duke University Medical Center, Durham, NC, USA. [5]Department of Medicine, Division of Infectious Diseases, Duke University Medical Center, Durham, NC, USA. [6]Department of Pediatrics, Weill Cornell Medicine, New York, NY, USA. [7]These authors contributed equally: Stephanie N. Langel, Francine L. Kelly, Maria Blasi, Scott M. Palmer. ✉email: maria.blasi@duke.edu

Fig. 1 Diacetyl (DA) vapor exposure of normal human bronchial epithelial cells (NHBECs) drives differential transcriptomic responses. **A** Schematic diagram of 3-hit model of PBS vehicle- and diacetyl (DA) vapor exposure of NHBECs. Triplicate wells of NHBECs from donor TBE-20 were exposed to PBS vehicle or DA vapor at 0, 2, and 4 days prior to RNA-seq analysis on day 6. **B** Volcano plot of RNA-seq results where genes are represented by red dots ($-\log_{10}$ adjusted P value < 0.001, $\log_2$ fold change > 1.5), blue dots ($-\log_{10}$ adjusted P value < 0.001, $\log_2$ fold change < 1.5), green dots ($-\log_{10}$ adjusted P value > 0.001, $\log_2$ fold change > 1.5), and black dots ($-\log_{10}$ adjusted P value > 0.001, $\log_2$ fold change < 1.5). **C** Down- and **D** upregulated gene ontology (GO) pathways with an FWER adjusted P value < 0.015 were reported. Dot size represents gene ratio and color schema represents FWER adjusted P values.

heatmap (Fig. S1A–C) of the differentially expressed genes (DEGs) demonstrate that DA vapor altered transcriptomic expression in NHBECs. To visualize the quantitative effects of DA vapor exposure in NHBECs, a volcano plot was generated in which the $\log_2$ fold change was plotted as a function of the negative log-transformed adjusted P value for all DEGs (Fig. 1B). To identify gene ontology (GO) and hallmark gene sets associated with altered expression after DA vapor exposure, gene set enrichment analysis (GSEA) was performed (1). We identified forty-five (Fig. 1C) and three (Fig. 1D) GO pathways that were significantly enriched among down- and

upregulated genes (using a stringent cutoff of FWER adjusted P value ≤ 0.01) after DA vapor exposure, respectively. Within the downregulated GO pathways (Table S1), we identified multiple genes that are required for cilia structure and motility (Fig. 2A, Table S2). These included proteins involved in the structure of the axoneme including dynein axonemal heavy chains (DNAHs), dynein cytoplasmic 2 heavy chains, dynein axonemal intermediate chains, and several transcripts for radial spokehead proteins (Fig. 2A, Table S2) [14]. Additionally, intraflagellar transport (IFT) genes, required for maintenance and formation of cilia, and
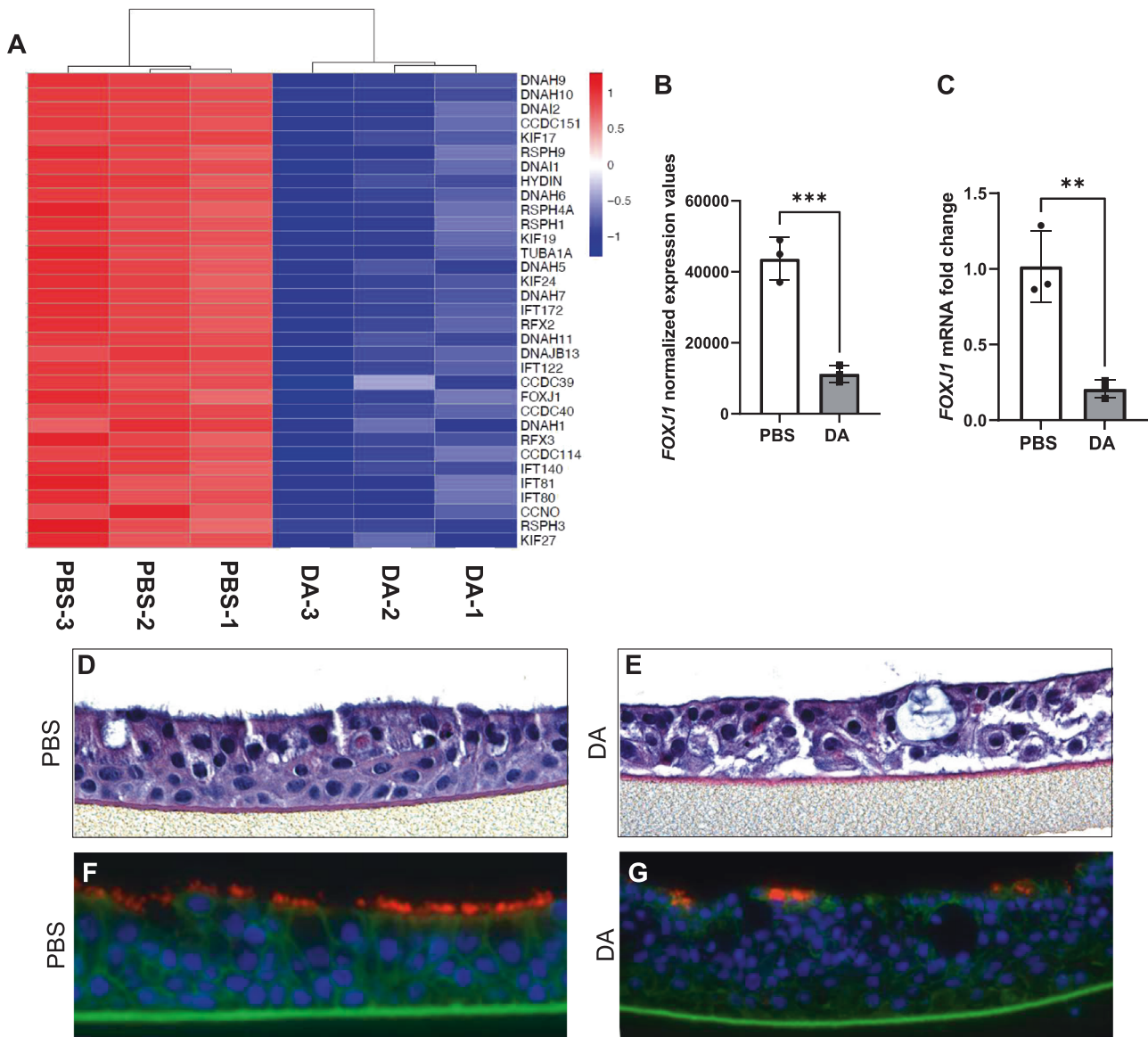
Fig. 2 Decreased expression of genes associated with cilia structure and motility in normal human bronchial epithelial cells (NHBECs) treated with diacetyl (DA) vapor. A Heatmap of DEGs that are downregulated following DA treatment and associated with cilia structure and motility. Red represents relative upregulation of gene expression and blue represents relative downregulation of gene expression. Genes are arranged by $\log_2$ fold change with the largest $\log_2$ fold change at the top and the smallest $\log_2$ fold change at the bottom. **B** *FOXJ1* normalized expression data from RNA-seq analysis. **C** Validation of *FOXJ1* expression by quantitative real-time polymerase chain reaction (qRT-PCR) shown as fold change after DA vapor exposure. **D** Pathological assessment after hematoxylin and eosin (H&E) staining of PBS vehicle and **E** DA vapor-exposed NHBECs. **F** Assessment of acetylated tubulin (red, Alex Fluor 594), β-catenin (green, Alex Fluor 488) and nuclei (blue, DAPI) expression in NHBECs via immunofluorescent staining after DA vapor or **G** PBS vehicle exposure. All quantified results are expressed as mean ± SD. $n = 3$ per group. Significance was determined by an unpaired t test. ****$P < 0.0001$, ***$P < 0.001$.

kinesin family member (KIF) genes, necessary for proper cilia structure, motility and length, were highly enriched in these downregulated GO pathways (Fig. 2A, Table S2) [15]. The transcription factor Forkhead box J1 (*FOXJ1*), required for multiciliated cell differentiation, along with transcriptional coactivators regulatory factor X (*RFX*)2 and *RFX3* [16] were also overrepresented in this analysis. We confirmed *FOXJ1* mRNA expression was significantly decreased in DA vapor—compared to PBS vehicle-exposed NHBECs via qRT-PCR (Fig. 2B, C). Assessment of hematoxylin and eosin staining in NHBECs demonstrated loss of cilia and flat dysplastic epithelium after DA vapor—compared to PBS vehicle exposure (Fig. 2D, E). Immunofluorescent staining of NHBECs revealed decreased expression of acetylated tubulin after DA vapor- compared to PBS vehicle exposure (Fig. 2F, G), further

validating the transcriptomic data demonstrating broad suppression of ciliogenesis after DA exposure.

DA vapor exposure increased CD14 and IL1B gene expression, HA production and promoted mobilization of NHBECs
Three of the most significantly upregulated GO pathways in response to DA exposure included Lipopolysaccharide (LPS) mediated signaling, Positive regulation of epithelial cell migration and Cellular response to mechanical stimulus. Within these GO pathways, we identified upregulated genes that fell within the stringent cutoff of our dataset (FWER adjusted P value < 0.001, $\log_2$ fold change > 1.5) (Table S3). Among these, included lymphocyte antigen 96 (LY96) [also known as myeloid differentiation factor 2 (MD-2) encoding protein MD2] and CD14, both
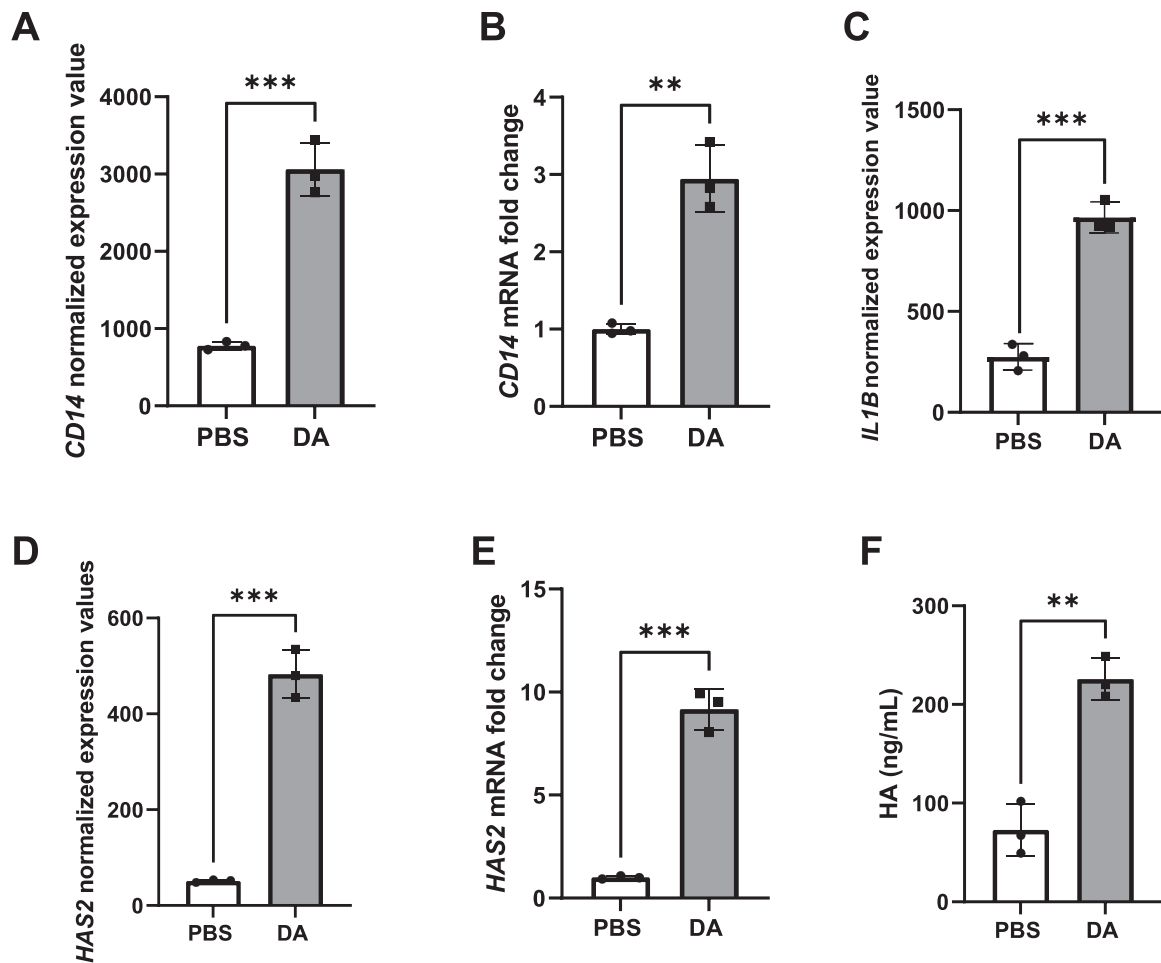
Fig. 3 DA vapor exposure increased *CD14*, *IL1B*, and hyalruonan synthase (*HAS2*) transcript expression as well as hyalruonan (HA) production in normal human bronchial epithelial cells (NHBECs). A *CD14* normalized expression data from RNA-seq analysis and **B** validation of *CD14* expression by quantitative real-time polymerase chain reaction (qRT-PCR) shown as fold change after PBS or DA vapor exposure. **C** *IL1B* normalized expression data from RNA-seq analysis. **D** *HAS2* normalized expression data from RNA-seq analysis and **E** validation of *HAS2* expression by qRT-PCR shown as fold change after PBS or DA vapor exposure. **F** Quantification of HA production in the NHBEC basal medium via ELISA. All quantified results are expressed as mean ± SD. $n = 3$ per group. Significance was determined by an unpaired t test. ***$P < 0.001$, **$P < 0.01$.

associated with TLR4-mediated LPS signaling [17] within the LPS mediated signaling GO pathway. Further validation by qRT-PCR indicated significant upregulation of CD14 mRNA in DA vapor- compared to PBS vehicle-exposed NHBECs, which corresponded to the normalized expression values from the RNA-seq analysis (Fig. 3A, B). IL1B, an inflammatory cytokine found in multiple upregulated GO pathways was significantly upregulated in DA vapor- compared to PBS vehicle-exposed cells (Fig. 3C). Within the Positive regulation of epithelial cell migration GO pathway, HAS2 was significantly upregulated gene both by normalized expression as determined by RNA-seq analysis (Fig. 3C) and mRNA levels from qRT-PCR (Fig. 3D). Notably, hyalruonan (HA) production in the NHBEC supernatant was also significantly increased after DA vapor rather than PBS vehicle exposure (Fig. 3E), further validating the HAS2 transcript data. Other transcripts associated with the Positive regulation of epithelial cell migration GO pathway including ITGA2, VEGF2, WNT7A and PTGS2 were expressed at high levels in NHBECs and were significantly higher after DA vapor compared to PBS vehicle exposure (Fig. 4A). Additionally, immunofluorescence staining demonstrates relocalization of basal cells throughout the pseudostratified epithelium in DA vapor- (Fig. 4C) compared to PBS vehicle-exposed (Fig. 4B) NHBECs.

Hallmark gene set analysis reveals pathways associated with interferon-alpha responses and DNA damage repair are downregulated while pathways associated with sterile inflammation are upregulated in NHBECs after DA vapor exposure

To further characterize transcriptional profiles, we applied the pre-ranked GSEA to 50 Hallmark gene sets with well-defined biological mechanisms and coherent expression levels. The Hallmark gene set analysis demonstrated that exposure to DA vapor resulted in enriched pathways amongst down- (Fig. S2A) and upregulated (Fig. S2B) genes, respectively. Similar to the GO pathways, Hallmark pathway analysis revealed a decrease in genes associated with interferon-alpha responses. Additionally, genes associated with E2F targets and the G2/M checkpoint associated with DNA replication and DNA damage repair, respectively, were downregulated after DA vapor exposure (Fig. S2A). Particularly relevant to DA-induced pattern recognition receptor (PRR) responses observed in the upregulated GO pathway analysis were Hallmark pathways associated with sterile inflammation (Table S4) including the *TNF-α signaling* via *NF-κB*, *Hypoxia*, *Inflammatory response*, and *IL-6 JAK STAT3 signaling* gene sets. Additionally, hypoxia induces p53 which mediates cellular apoptosis [18], both of which were upregulated in the Hallmark

A

Gene	Gene name	Gene Function	Log2 fold change	Adjusted p-value	Average PBS	Average DA
HAS2	Hyaluronan synthase 2	Regulates synthesis of hyaluronan	3.23	7.29E-68	51.47	482.91
ITGA2B	Integrin subunit alpha 2	Receptor for laminin, collagen, fibronectin, E-cadherin	2.74	7.03E-10	10.03	66.78
TEK	TEK Receptor tyrosine kinase	Angiopoietin-1 receptor	2.55	8.58E-16	22.04	130.72
FGF2	Fibroblast growth factor 2	Fibroblast growth and heparin binding	2.49	6.14E-21	34.72	193.43
KDR	Vascular endothelial growth factor receptor 2 (VEGF2)	Promotes cellular proliferation and migration	2.37	2.07E-55	249.80	1290.13
INSL3	Insulin like-3	Promotes cellular migration	1.86	2.65E-14	41.84	151.02
WNT7A	Protein Wnt-7a	Canonical Wnt/beta-catenin signaling pathway, promotes cellular migration	1.68	2.94E-31	505.51	1622.12
PTGS2	Prostaglandin G/H synthase 2	Mediates responses to sterile and infectious inflammation	1.47	5.47E-29	1831.63	5088.94
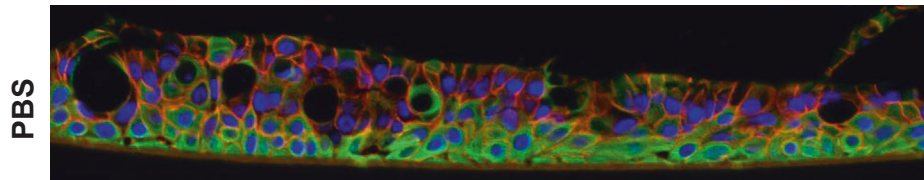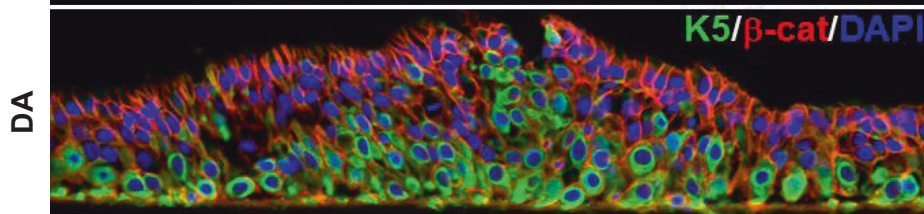
Fig. 4 DA vapor exposure induces an epithelial cell mobilization phenotype. A Upregulated genes from the *Positive regulation of epithelial cell migration* gene ontology pathway that fell within the stringent cutoff of our dataset (FWER adjusted *P* value < 0.001, $\log_2$ fold change >1.45) **B** Representative confocal images of keratin 5 (K5, green, Alex Fluor 488), β-catenin (green, Alex Fluor 59) and nuclei (blue, DAPI) expression in NHBECs via immunofluorescent staining after PBS vehicle or **C** DA vapor exposure.

gene set analysis (i.e., *P53 pathway* and *Apoptosis*). *Kras* and *TGF-β signaling* pathways associated with repair were also included in the significantly upregulated gene sets after Hallmark gene set analysis. Overall, Hallmark pathways associated with sterile inflammation and repair were both upregulated after DA exposure.

Decreased expression of multiple ISGs after DA vapor exposure

In both the GO and Hallmark gene set pathway analyses, interferon responses were enriched among the downregulated pathways. To further evaluate the effect of DA vapor exposure on innate immune factors important in antiviral protection of epithelial cells, we identified DEGs of the interferon stimulated gene (ISG) family (FWER adjusted *P* value ≤ 0.01) after DA vapor exposure (Fig. 5A, Table S5). DA vapor exposure in NHBECs downregulated expression of ISGs previously demonstrated to suppress replication of both RNA and DNA viruses (Fig. 5A) [19]. Radical SAM domain-containing 2 [RSAD2 (also known as Viperin)], a potent antiviral ISG, was one of the most negatively DEG impacted by DA vapor exposure. RSAD2 mRNA expression was further validated by qRT-PCR was found to be significantly lower in DA vapor-compared to PBS vehicle-exposed NHBECs, which corresponded to normalized expression values from the RNA-seq analysis (Fig. 5B, C). Additionally, multiple chemotactic factors involved in the recruitment of immune cells were significantly downregulated (Table S5). The suppression of multiple ISGs and chemotactic factors after DA vapor exposure suggests increased susceptibility to viral infection in NHBECs.

DA vapor exposure increases susceptibility of NHBECs to SARS-CoV-2 infection

We first determined if DA vapor exposure alters expression of SARS-CoV-2 receptor ACE2 and transmembrane serine protease 2

(TMPRSS2), a cellular protease required for SARS-CoV-2 entry. Despite the negative impact of DA on NHBEC morphology and decrease in cilia, IHC staining confirmed that DA vapor did not ameliorate ACE2 or TMPRRS2 expression (Fig. 6A), suggesting that SARS-CoV-2 could still bind and enter DA vapor-exposed NHBECs. To determine the impact of DA vapor exposure on SARS-CoV-2 susceptibility, NHBECs were first exposed to PBS vehicle or DA vapor for 1 h on days 0, 2, and 4, and infected with SARS-CoV-2 USA-WA1/2020 (MOI of 0.5), after 24 h of the final DA exposure. As measures of viral infection and replication, we determined both cell-free (Fig. 6B) and cell-associated (Fig. 6C, D) viral RNA levels after 48 h of infection. DA vapor exposure significantly increased viral replication in NHBECs, as indicated by total viral RNA release in apical media (Fig. 6B) and genomic (Fig. 6C) and subgenomic (Fig. 6D) viral RNA levels. SARS-CoV-2 infection did not further exacerbate cell dysplasia or cilia loss in DA vapor-exposed NHBECs (Fig. S3). Our data indicated an increased susceptibility of NHBECs to SARS-CoV-2 infection.

DISCUSSION

Damage to airway epithelium caused by cigarette smoking, environmental pollutants, and pathogenic infections, amongst others, is associated with cilia loss and inflammation in the airway epithelium [20–23]. Emerging evidence also suggests that these factors increase susceptibility to SARS-CoV-2 infection and COVID-19 [24–28]. Whether DA also impacts susceptibility to SARS-CoV-2 infection and/or COVID-19 severity is not well established. Recent studies suggest that flavoring chemicals like DA have direct toxicity to airway cells and could contribute to adverse health outcomes [29–31]. Specifically, DA vapor exposure causes loss of epithelial resistance, flattening of the airway epithelium, and loss of cilia in both in vitro and in vivo models [32].
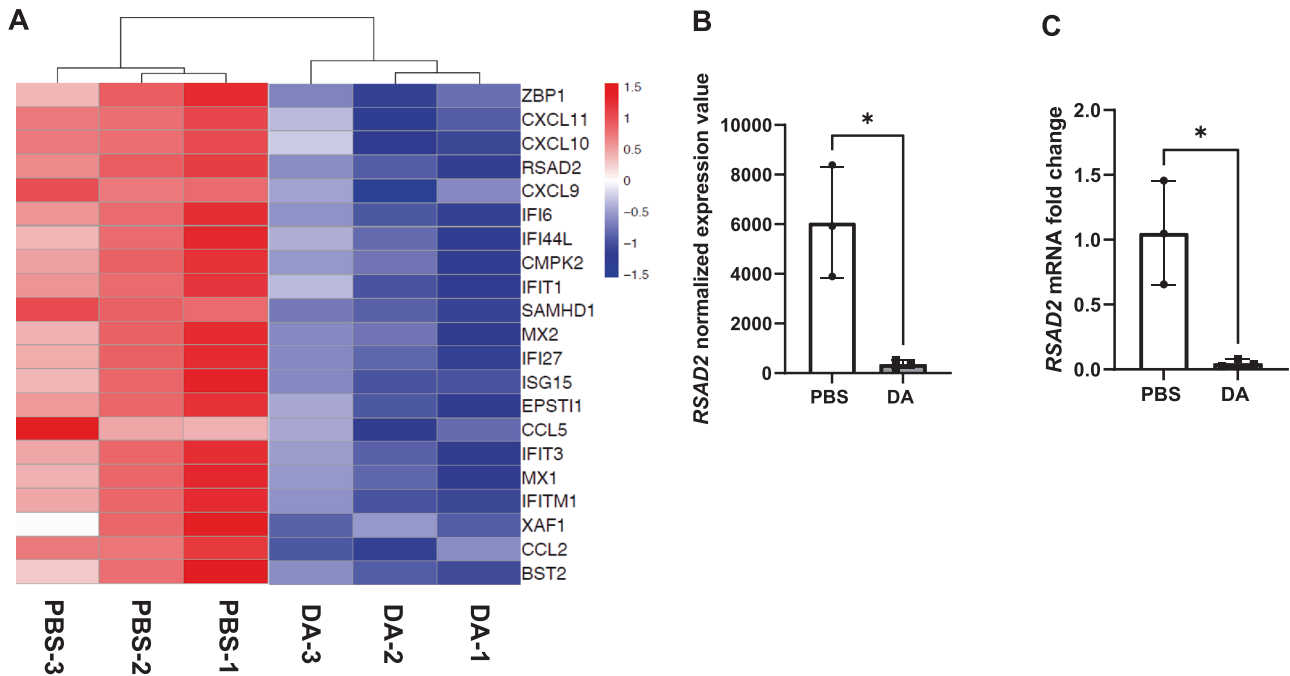
Fig. 5 Decreased expression of interferon-stimulated genes after diacetyl (DA) vapor exposure in normal human bronchial epithelial cells (NHBECs). A Heatmap of interferon-stimulated genes that are downregulated following DA treatment. Red represents relative upregulation of gene expression and blue represents relative downregulation of gene expression. Genes are arranged by $\log_2$ fold change with the largest $\log_2$ fold change at the top and the smallest $\log_2$ fold change at the bottom. **B** RSAD2 normalized expression data from RNA-seq analysis and **C** validation of RSAD2 expression by qRT-PCR shown as fold change after DA vapor exposure. All quantified results are expressed as mean ± SD. $n = 3$ per group. Significance was determined by an unpaired t test. *$P < 0.05$.
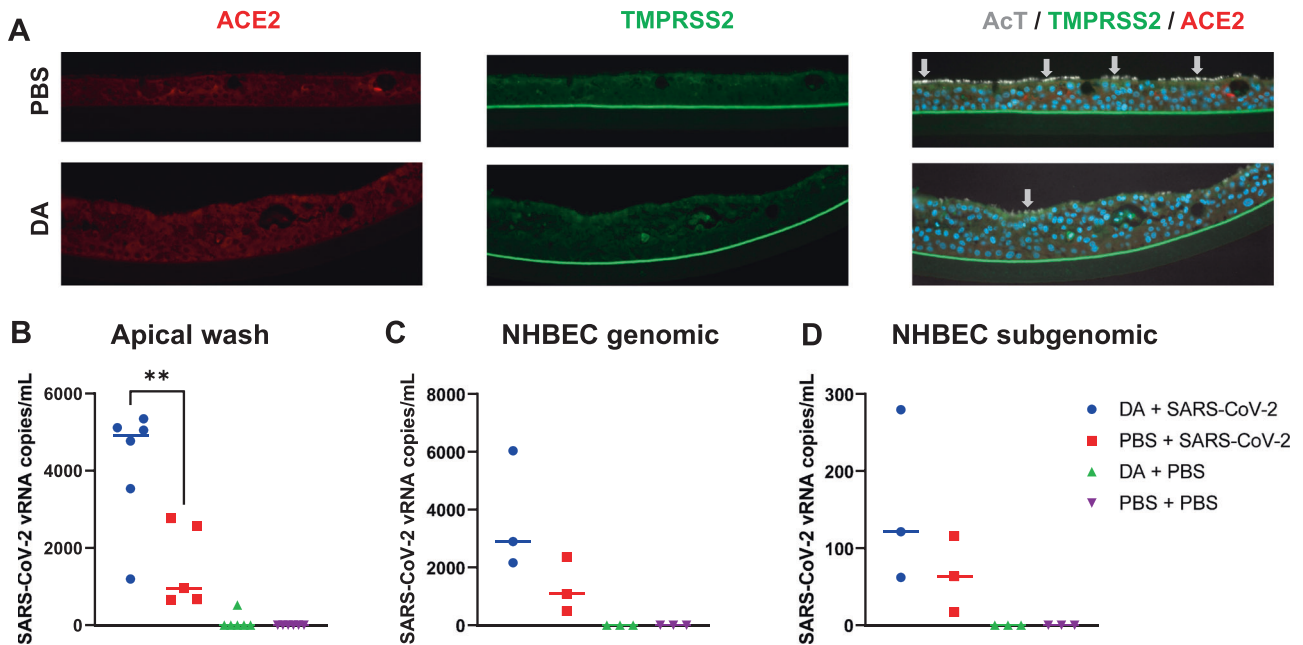
Fig. 6 DA treatment does not alter ACE2 receptor or TMPRSS2 cellular protease expression but increases normal human bronchial epithelial cell (NHBEC) susceptibility to SARS-CoV-2 infection. A Immunofluorescence was performed on cross sections of formalin-fixed and paraffin-embedded NHBECs to visualize ACE2 (red, Alex Fluor 594), TMPRRS2 (green, Alex Fluor 488), acetylated tubulin (AcT, gray), and nuclei (blue, DAPI). Images are captured at 20X magnification. Total SARS-CoV-2 RNA levels were determined in **B** apical wash and **C** genomic and **D** subgenomic viral RNA levels were determined in NHBECs. Data points represent replicates from one NHBEC donor. Significance was determined by a one-way ANOVA with Tukey's corrections for multiple comparisons. **$P < 0.01$.

Airway epithelium contain motile cilia which are an integral part of the mucociliary escalator, removing fluids, mucins, and particulates from the airway [33, 34]. Previous evidence demonstrates that expression of multiple genes involved in cilia biogenesis are significantly downregulated in NHBECs when DA liquid was added to cell culture media [29]. Similarly, we observed loss of cilia on the surface of NHBECs and broad suppression of transcripts related to cilia structure and function after DA vapor

exposure. For example, *FOXJ1*, a master regulator of motile ciliogenesis [35, 36], and *RFX2* and *RFX3*, transcriptional coactivators of FoxJ1 [16, 37], were significantly downregulated in our RNA-seq analysis. Considering cilia assembly is under strict transcriptional control, DA-induced suppression of these transcripts could result in an overall decrease in the cell's cilia production program. Other transcripts overrepresented in the top 10 downregulated pathways were associated with the radial spoke and spokehead, dynein proteins, IFT proteins KIF member genes and *CCNO*, *HYDIN* and *TUBA1A* transcripts. We further validated the transcriptomic data and observed loss of cilia by cell histology and decreased protein expression of acetylated tubulin. Acetylation of α-tubulin marks stable, long-lived subpopulations of cilia and flagella, and decreased acetylated tubulin indicates primary cilia loss [38]. The suppression of cilia-related genes in addition to cilia loss is likely to result in decreased mucociliary clearance and increased cellular susceptibility to pathogens. Indeed, genetic defects in *DNAH5, HYDIN,* and *TUBA1A* and others result in primary cilia dyskinesia (PCD); a variety of clinical manifestations including ineffective mucociliary clearance and recurrent lower respiratory tract infections [39–48].

Various endogenous danger-associated molecular patterns (DAMPs) are produced after non-pathogenic cellular injury that activate PRRs and induce sterile inflammation [49]. HA is an extracellular matrix glycosaminoglycan released after sterile injury or pathogenic infection and exerts size-dependent effects. For example, low molecular weight (LMW) HA acts as a proinflammatory DAMP via toll-like receptor (TLR) signaling [50, 51]. We demonstrated that DA exposure increased *HAS2* transcript expression and HA production in NHBECs. While we did not measure LMW HA specifically, we observed an increase in transcripts associated with PRR signaling. For example, *CD14* and *LY96* gene expression were significantly upregulated after DA treatment. Membrane-bound CD14 is a PRR that recognizes diverse microbial products [52–56] and LY96 (MD-2) physically associates with TLR4 to mediate LPS signaling via CD14 [17]. Interestingly, HA is demonstrated to signal through a unique complex of TLR4, MD-2 and CD44 [57]. While HA has not been demonstrated to signal through CD14 directly, the interaction of HA binding proteoglycans like versican and CD14 can stimulate downstream cellular responses [58–60]. Additionally, HA exudates have been observed in the lungs of deceased COVID-19 patients [61, 62], suggesting a role for this molecule in acute respiratory distress syndrome caused by SARS-CoV-2. We also observed mobilization of NHBECs after DA vapor exposure. After mechanical damage to airway epithelium, epithelial cell migration is integral to tissue repair [63]. Previous studies demonstrate that rats that inhale DA exhibit ultrastructural changes in the trachea consistent with epithelial spreading and migration [64]. Interestingly, increased basal cell mobilization is also observed during SARS-CoV-2 infection in NHBECs in vitro [65]. Altogether these results suggest that damage to the airway epithelium, whether by toxin exposure or viral infection, results in epithelial cell mobilization that will impact the processes involved in epithelium repair.

We identified downregulated Hallmark pathways associated with DNA replication and DNA damage repair after DA exposure. This is consistent with previous literature demonstrating DA covalently binds to guanyl nucleotides leading to DNA unwinding and cellular apoptosis [66]. Damage is likely further exacerbated by an increase in DA-induced hypoxia and sterile inflammation as indicated in our Hallmark pathway analysis. Recent studies have demonstrated a link between hypoxia and sterile inflammation via IL-1β priming of the NLRP3 inflammasome [67–71]. The upregulation of the *Hypoxia* and *Inflammatory response* Hallmark pathways and significant increase in the *IL1B* gene observed in our RNA-seq analysis suggests a similar mechanism after DA exposure in NHBECs. Hypoxia induces p53 which mediates cellular apoptosis [18], both of which are upregulated in the Hallmark gene set

analysis (i.e. *P53 pathway* and *Apoptosis*). Furthermore, the upregulation of *TNF-α signaling* via *NF-κB* and *IL-6 JAK STAT3 signaling* Hallmark pathways highlight a potential role for TNF-α and IL-6 as triggers of sterile inflammation as previously demonstrated [72, 73]. The increase in *Kras* and *TGF-β signaling* pathways after DA vapor exposure suggests a role for TGF-β in mediating tissue remodeling after hypoxia-induced injury [74]. KRAS is a member of the Ras protein family, which functions as a signal transducer between epidermal growth factor receptor (EGFR) signaling and the MAPK pathway (Ras/MAPK pathway) [75]. Ras/MAPK activity induces p53 phosphorylation, enabling the interaction of p53 and TGF-β. Overall, the Hallmark gene set analysis suggests that DA vapor exposure results in changes in NHBECs similar to those observed in hypoxia leading to inflammation and compensatory TGF-β-mediated repair signatures.

We observed suppression of multiple ISG transcripts important in antiviral protection of epithelial cells after DA vapor exposure in NHBECs. ISG products exhibit many diverse functions but collectively are highly effective at resisting and controlling viral infections [76]. For example, RSAD2 (Viperin) was one of the most significantly decreased ISG after DA vapor exposure. Viperin has been demonstrated to inhibit replication of multiple respiratory viruses including measles, respiratory syncytial virus, and influenza [77–79]. Previous studies demonstrate that e-cig exposure significantly impaired antiviral host defenses in the lung [9, 10]. Ours is the first evidence that a flavoring chemical directly reduces expression of multiple ISG transcripts in NHBECs. These data demonstrate that DA suppressed the transcriptomic expression of important antiviral and immune factors that could lead to increased susceptibility to SARS-CoV-2.

The evidence that DA exposure induces a loss of cilia and acetylated tubulin combined with a decrease in transcriptomic expression of important ISGs led us to hypothesize that DA vapor-exposed NHBECs cells would be more susceptible to SARS-CoV-2 infection. Indeed, recent evidence demonstrates a loss of motile cilia and dedifferentiation of the epithelial cells after SARS-CoV-2 infection both in vitro and in vivo [65]. After confirming SARS-CoV-2 receptor ACE2 and cellular protease TMPRSS2 were still present after DA vapor exposure, we infected DA vapor and PBS vehicle-exposed NHBECs with SARS-CoV-2. The increase in the mean of both genomic and subgenomic SARS-CoV-2 RNA levels in NHBECs demonstrate that DA increases susceptibility of NHBECs to SARS-CoV-2 infection. These data are in line with a recent report demonstrating that direct cigarette smoke exposure reduces innate immune responses and increases the number of SARS-CoV-2 infected cells [25]. Additionally, this is consistent with other studies demonstrating negative impacts of e-cigs on the airway and host defenses. For example, mice exposed to e-cig vapor had altered lung lipid homeostasis and downregulated innate immune responses in alveolar macrophages and epithelial cells. When infected with influenza, e-cig vapor-exposed mice had increased lung inflammation and tissue damage [11]. Our data demonstrate that DA vapor induces cilia loss and specific pathological changes in the airway epithelium that increase susceptibility to viral infection, specifically against SARS-CoV-2, suggesting a potential mechanism for increased susceptibility in e-cigarette users.

METHODS
EpiAirway tissues and vapor exposure
Fully differentiated human EpiAirway tissue inserts (0.6 cm^2) were purchased from MatTek Corporation (Ashland, MA). EpiAirway tissues were generated from lower tracheal/bronchial cells (AIR-112-D2; TBE-20, (healthy, non-smoker, 13 yo male donor), and cultured at the air-liquid interface (ALI) at 37 °C (+5% CO$_2$). Upon receipt, EpiAirway tissue inserts were placed into 1 mL of culture medium (MatTek) in 6 well culture plates for 16–18 h to equilibrate. The apical surface was then gently rinsed 2X

with 0.4 mL PBS (MatTek) to remove excess mucus. The tissue inserts were transferred into 1 mL of fresh culture medium, which bathes the basolateral side of the tissue, and exposed to the apical surface to DA vapor for 1 h at 37 °C (+5% CO_2) using vapor cups (MatTek). Specifically, 50 µl of PBS vehicle or 25 mM DA (104 µg/1100 ppm), was applied to a fiber pad in a vapor cup supplied by MatTek (AIR-1488 MILCEL-MTK-CAP-FP) which was then inverted and sealed (using silicone) on the tissue insert for 1 h, as previously described [4]. Tissue inserts were exposed to vehicle or DA vapor for 1 h on days 0, 2, and 4. The apical surface was rinsed twice with PBS prior to vapor exposure. The culture medium was collected every day and replaced with 1 mL of fresh medium. Basolateral supernatants were collected, centrifuged at 15,000 × g for 15 min at 4 °C to remove cellular debris, and stored at −80 °C until evaluation. Cells were washed, then frozen at −80 °C at day 6, 48 h after the last exposure, to preserve cells for future transcript analysis.

RNA isolation and transcript analysis
Cells were lysed in 350 µl of Trizol, and RNA was extracted by phenol: chloroform method, and collected over RNAeasy column (Qiagen, Germantown, MD). Seven microliters of RNA was converted to cDNA using the high capacity reverse transcription kit (LifeTech, Carlsbad, CA). Transcripts were evaluated by TaqMan assay, where 40 ng of cDNA was used in each reaction with validated assays, and duplexed with β actin as the endogenous control. Ct values were determined using ABI 7500 RealTime PCR System (LifeTech, Carlsbad, CA) with SDS software version 1.5.1. Change in expression was calculated using the $2^{-\Delta\Delta Ct}$ method.

HA ELISA
Clarified basolateral supernatants were evaluated for HA production using an HA ELISA (R&D Systems, Inc., Minneapolis, MN), following the manufacturer's protocol.

EpiAirway staining
EpiAirway tissue inserts were washed twice with 1× PBS, fixed with 10% formalin, and embedded in paraffin. Five micrometers sections were evaluated by immunofluorescence following deparaffinization and citrate buffer antigen retrieval. Sections were blocked with 5% BSA in PBS for 1 h at room temperature, primary and secondary antibodies were diluted in blocking solution and incubated overnight at 4 °C or room temperature for 90 min, respectively. Following secondary antibody, slides were washed in PBS and cover-slipped with DAPI in Fluoromount G mounting media (Southern Biotech, Birmingham, AL). Images were obtained using a Oberserver Z1 Zeiss microscope (Dublin, CA) equipped with a digital camera and processed using Zen-Pro (Dublin, CA). Primary antibodies used and their concentrations are as follow: mouse IgG1 anti-β catenin (1:400, BD, Franklin Lakes, New Jersey), mouse IgG2b anti-acetylated tublin (AcT) (1:10,000, Sigma, St Louis, MO), mouse IgG1 anti-TMPRSS2 (1:25, EMD Millipore, Temecula, CA), rabbit anti-ACE2 (1:50, Abcam, Cambridge, MA). Secondary antibodies used and their concentrations are as follows: Goat anti-IgG1 Alexa Fluor 488 (1:500, LifeTech, Carlsbad, CA), goat anti-IgG2b Alexa Fluor 594, 680 (1:500, LifeTech, Carlsbad, CA), donkey anti-rabbit Alexa Fluor 488 (1:500, LIfeTech, Carlsbad, CA)

SARS-CoV-2 propagation and tittering
SARS-CoV-2 USA-WA1/2020 (BEI Resources) was propagated on Vero E6 cells (passage 1–2) at a multiplicity of infection (MOI) = 0.001 in virus diluent [DMEM supplemented with 2% FBS, 1× Penicillin/Streptomycin (Gibco), 1 mM sodium pyruvate (Gibco) and 1× NEAA (Gibco) at 37 °C in 5% CO_2. At day 4 post infection, cell supernatant containing the released virus was harvested, centrifuged at 500 × g for 5 min, filtered through a 0.22 µM sterile vacuum filtration system, aliquoted and stored at −80 °C until further use.

Stock viral titer was determined by plaque assay. Briefly, 0.72 × 10^5 Vero E6 cells were seeded in 6 well plates. The stock virus was serially diluted and incubated on cellular monolayer at 37 °C in 5% CO_2. After 1 h, virus was aspirated, and cells were overlayed with carboxy-methyl cellulose (CMC) containing media 0.6% CMC, MEM supplemented with 1× Penicillin/Streptomycin (Gibco), 2% FBS, 1 mM sodium pyruvate (Gibco), 1× NEAA (Gibco), 0.3% sodium bicarbonate (Gibco), and 1× GlutaMAX (Gibco). After 4 days of incubation at 37 °C in 5% CO_2, plaque assays were stained with 1% crystal violet in 10% neutral buffered formalin (NBF), and plaque forming unit/mL (PFU/mL) was determined.

SARS-CoV-2 infection
One day after the third DA vapor exposure (day 5), the apical side of NHBECs cells were washed 1× with PBS and incubated with either SARS-CoV-2 at an MOI of 0.5 or PBS at 37 °C and 5% CO_2, with intermittent plate rocking. At 48 h post SARS-CoV-2 inoculation, apical cell washes and cells were lysed in trizol for RNA isolation and viral analyses.

qRT-PCR for detecting viral RNA
After 48 h of infection, NHBECs were resuspended in TRIzol reagent (Thermo Fisher). Cellular RNA was extracted by phase separation with chloroform and subsequently using the RNeasy Mini Kit (Qiagen). RNA from cell supernatants was extracted using the QIAamp viral RNA mini kit (Qiagen). A two-step qRT-PCR was used to detect viral RNA released in the cell supernatant. In the first step, viral cDNA for the nucleocapsid (N) gene was generated using SuperScript III Reverse Transcriptase (Invitrogen), following manufacturer's instructions. For cDNA preparation of genomic and sub-genomic viral RNA, N-reverse primer (5′-GAGGAACGAGAAA-GAGGCTTG-3′) and N-forward primer (5′-CACATTGGCACCCGCAATC-3′) were used, respectively.

In the second step, 7 µl cDNA from step-1 was amplified using N gene forward primer (5′-CACATTGGCACCCGCAATC-3′), N gene reverse primer (5′-GAGGAACGAGAAGAGGCTTG-3′) and probe (5″-FAM-ACTTCCTCAAG-GAACAACATTGCCA-QSY-3′) using Taqman mastermix (Thermo Fisher). The thermal cycling steps were: 50 °C for 2 min, 95 °C for 10 min, and 40 cycles of 95 °C for 15 s and 60 °C for 1 min, and qPCR was performed on a Step-One-Plus real-time PCR machine (Applied Biosystems) using the StepOne Software v2.3.

Viral RNA copy number/mL supernatant was assessed using pCDNA3.1 (+)-N-eGFP plasmid (GenScript) as standard. We determined the copy number by using the following formula:

$$\text{Number of copies (molecules)} = \frac{X \text{ ng} * 6.0221 \times 10^{23} \text{ molecules/mole}}{(N * 660 \text{ g/mole})^{\dagger} * 1 \times 10^{9} \text{ ng/g}}$$

and the following link was used to calculate the final copy number: http://www.scienceprimer.com/copy-number-calculator-for-realtime-pcr.

Generation and analysis of the bulk-RNA-seq data
Total RNA was isolated from cells using RNeasy Plus Mini kit (Qiagen) according to manufacturer's instructions. The RNA concentration and integrity was determined on the NanoDrop ND-1000 (Thermo Fisher Scientific). One thousand nanograms RNA from each sample was used as a template for preparing Illumina compatible libraries using the TruSeq RNA Library Prep Kit v2 (Illumina). Library sizes were checked using D5000 high sensitivity tape on the TapesSation 2200 (Agilent), and pooled libraries concentration were determined by Qubit 3.0 Fluorometer (Thermo Fisher Scientific). A library input of 1.8 pM with 1% PhiX (Illumina) spike-in was sequenced using the NextSeq 500 instrument (Illumina) with the NextSeq 500/550 High Output v2.5 Kit (Illumina).

RNA-Seq data were quality checked with FastQC [80] and preprocessing was carried out using TrimGalore [81] toolkit to trim low-quality bases and Illumina adapter sequences using default values. Reads were aligned to the ENSEMBL Homo_sapiens.GRCh38.dna.primary_assembly genome using the ENSEMBL Homo_sapiens.GRCh38.100 transcript [82] annotation file with STAR [83] splice-aware RNA-seq alignment tool in paired mode allowing maximum multimapping of 3. Gene level counts were quantified using FeatureCounts [84] tool, counting unique features in non-stranded mode and retaining both gene ID, gene name, and gene biotype mapping from the ENSEMBL annotation file. Prior to differential expression analysis, count data was collapsed to donor level and genes for which mean raw count was at least 15 were kept. Normalization and differential expression were carried out with DESeq2 [85] Bioconductor [86] package, utilizing the 'apeglm' Bioconductor package [87] for log fold change shrinkage, in R statistical programming environment. The design formula was constructed to test for the effect of treatment while controlling for donor.

The RNA-seq data was processed using the TrimGalore toolkit [1] which employs Cutadapt [2] to trim low-quality bases and Illumina sequencing adapters from the 3′ end of the reads. Only reads that were 20nt or longer after trimming were kept for further analysis. Reads were mapped to the GRCh38v93 version of the human genome and transcriptome [3] using the STAR RNA-seq alignment tool [4]. Reads were kept for subsequent analysis if they mapped to a single genomic location. Gene counts were compiled using the HTSeq tool [5]. Only genes that had at least 10 reads in any given

library were used in subsequent analysis. Normalization and differential expression was carried out using the DESeq2 [6] Bioconductor [7] package with the R statistical programming environment [8]. The false discovery rate was calculated to control for multiple hypothesis testing. GSEA [9] was performed to identify GO terms and pathways associated with altered gene expression for each of the comparisons performed.

Statistics

For all qRT-PCR experiments, unpaired t tests were used. Additionally, an ordinary 1-way ANOVA with Tukey's multiple comparison test was used to compared SARS-CoV-2 viral RNA levels between the experimental groups. All analyses were performed using GraphPad Prism 9 (La Jolla, CA).

Biocontainment and biosafety

Biocontainment work for SARS-CoV-2 was performed with approved standard operating procedures in the Duke Regional Biocontainment Laboratory.

DATA AVAILABILITY

The data that support the findings of this study are available from the corresponding authors upon request.

REFERENCES

1. Allen JG, Flanigan SS, LeBlanc M, Vallarino J, MacNaughton P, Stewart JH, et al. Flavoring chemicals in e-cigarettes: diacetyl, 2,3-pentanedione, and acetoin in a sample of 51 products, including fruit-, candy-, and cocktail-flavored e-cigarettes. Environ Health Perspect. 2016;124:733–9.
2. Muthumalage T, Prinz M, Ansah KO, Gerloff J, Sundar IK, Rahman I. Inflammatory and oxidative responses induced by exposure to commonly used e-cigarette flavoring chemicals and flavored e-liquids without nicotine. Front Physiol. 2017;8:1130.
3. Kelly FL, Weinberg KE, Nagler AE, Nixon AB, Star MD, Todd JL, et al. EGFR-dependent IL8 production by airway epithelial cells after exposure to the food flavoring chemical 2,3-butanedione. Toxicol Sci. 2019;169:534–42.
4. Kelly FL, Sun J, Fischer BM, Voynow JA, Kummarapurugu AB, Zhang HL, et al. Diacetyl induces amphiregulin shedding in pulmonary epithelial cells and in experimental bronchiolitis obliterans. Am J Respir Cell Mol Biol. 2014;51:568–74.
5. Brass DM, Gwinn WM, Valente AM, Kelly FL, Brinkley CD, Nagler AE, et al. The diacetyl-exposed human airway epithelial secretome: new insights into flavoring-induced airways disease. Am J Respir Cell Mol Biol. 2017;56:784–95.
6. Foster MW, Gwinn WM, Kelly FL, Brass DM, Valente AM, Moseley MA, et al. Proteomic analysis of primary human airway epithelial cells exposed to the respiratory toxicant diacetyl. J Proteome Res. 2017;16:538–49.
7. Kreiss K. Recognizing occupational effects of diacetyl: What can we learn from this history? Toxicology. 2017;388:48–54.
8. Gaiha SM, Cheng J, Halpern-Felsher B. Association between youth smoking, electronic cigarette use, and coronavirus disease 2019. J Adolesc Health. 2020;67:519–23.
9. Sussan TE, Gajghate S, Thimmulappa RK, Ma J, Kim JH, Sudini K, et al. Exposure to electronic cigarettes impairs pulmonary anti-bacterial and anti-viral defenses in a mouse model. PLoS ONE. 2015;10:e0116861.
10. Ghosh A, Coakley RD, Ghio AJ, Muhlebach MS, Esther CR Jr, Alexis NE, et al. Chronic e-cigarette use increases neutrophil elastase and matrix metalloprotease levels in the lung. Am J Respir Crit Care Med. 2019;200:1392–401.
11. Madison MC, Landers CT, Gu BH, Chang CY, Tung HY, You R, et al. Electronic cigarettes disrupt lung lipid homeostasis and innate immunity independent of nicotine. J Clin Investig. 2019;129:4290–304.
12. Tay MZ, Poh CM, Rénia L, MacAry PA, Ng LFP. The trinity of COVID-19: immunity, inflammation and intervention. Nat Rev Immunol. 2020;20:363–74.
13. Mason RJ. Pathogenesis of COVID-19 from a cell biology perspective. Eur Respir J. 2020;55:2000607.
14. Satir P, Christensen ST. Overview of structure and function of mammalian cilia. Annu Rev Physiol. 2007;69:377–400.
15. Nakayama K, Katoh Y. Ciliary protein trafficking mediated by IFT and BBSome complexes with the aid of kinesin-2 and dynein-2 motors. J Biochem. 2017;163:155–64.
16. Didon L, Zwick RK, Chao IW, Walters MS, Wang R, Hackett NR, et al. RFX3 modulation of FOXJ1 regulation of cilia genes in the human airway epithelium. Respir Res. 2013;14:70.
17. Shimazu R, Akashi S, Ogata H, Nagai Y, Fukudome K, Miyake K, et al. MD-2, a molecule that confers lipopolysaccharide responsiveness on Toll-like receptor 4. J Exp Med. 1999;189:1777–82.
18. Leszczynska KB, Foskolou IP, Abraham AG, Anbalagan S, Tellier C, Haider S, et al. Hypoxia-induced p53 modulates both apoptosis and radiosensitivity via AKT. J Clin Investig. 2015;125:2385–98.
19. Schoggins JW. Interferon-stimulated genes: what do they all do? Annu Rev Virol. 2019;6:567–84.
20. Simet SM, Sisson JH, Pavlik JA, Devasure JM, Boyer C, Liu X, et al. Long-term cigarette smoke exposure in a mouse model of ciliated epithelial cell function. Am J Respir Cell Mol Biol. 2010;43:635–40.
21. Leopold PL, O'Mahony MJ, Lian XJ, Tilley AE, Harvey B-G, Crystal RG. Smoking is associated with shortened airway cilia. PLoS ONE. 2009;4:e8157–e8157.
22. Cao Y, Chen M, Dong D, Xie S, Liu M. Environmental pollutants damage airway epithelial cell cilia: Implications for the prevention of obstructive lung diseases. Thorac Cancer. 2020;11:505–10.
23. Smith CM, Kulkarni H, Radhakrishnan P, Rutman A, Bankart MJ, Williams G, et al. Ciliary dyskinesia is an early feature of respiratory syncytial virus infection. Eur Respir J. 2014;43:485–96.
24. CDC. People with certain medical conditions. COVID-19. 2020. https://www.cdc.gov/coronavirus/2019-ncov/need-extra-precautions/people-with-medical-conditions.html
25. Purkayastha A, Sen C, Garcia G Jr, Langerman J, Shia DW, Meneses LK, et al. Direct exposure to SARS-CoV-2 and cigarette smoke increases infection severity and alters the stem cell-derived airway repair response. Cell Stem Cell. 2020;27:869–75.e864.
26. Wu X, Nethery RC, Sabath MB, Braun D, Dominici F. Air pollution and COVID-19 mortality in the United States: strengths and limitations of an ecological regression analysis. Sci Adv. 2020;6:eabd4049.
27. Leung JM, Niikura M, Yang CWT, Sin DD. COVID-19 and COPD. Eur Respir J. 2020;56:2002108.
28. Organization WH. Smoking and COVID-19. 2020. https://www.who.int/news-room/commentaries/detail/smoking-and-covid-19
29. Park HR, O'Sullivan M, Vallarino J, Shumyatcher M, Himes BE, Park JA, et al. Transcriptomic response of primary human airway epithelial cells to flavoring chemicals in electronic cigarettes. Sci Rep. 2019;9:1400.
30. Palmer SM, Flake GP, Kelly FL, Zhang HL, Nugent JL, Kirby PJ, et al. Severe airway epithelial injury, aberrant repair and bronchiolitis obliterans develops after diacetyl instillation in rats. PLoS ONE. 2011;6:e17644.
31. Morgan DL, Jokinen MP, Price HC, Gwinn WM, Palmer SM, Flake GP. Bronchial and bronchiolar fibrosis in rats exposed to 2,3-pentanedione vapors: implications for bronchiolitis obliterans in humans. Toxicol Pathol. 2012;40:448–65.
32. Brass DM, Palmer SM. Models of toxicity of diacetyl and alternative diones. Toxicology. 2017;388:15–20.
33. Bustamante-Marin XM, Ostrowski LE. Cilia and mucociliary clearance. Cold Spring Harb Perspect Biol. 2017;9:a028241.
34. Kuek LE, Lee RJ. First contact: the role of respiratory cilia in host-pathogen interactions in the airways. Am J Physiol Lung Cell Mol Physiol. 2020;319:L603–19.
35. You Y, Huang T, Richer EJ, Schmidt JE, Zabner J, Borok Z, et al. Role of f-box factor foxj1 in differentiation of ciliated airway epithelial cells. Am J Physiol Lung Cell Mol Physiol. 2004;286:L650–57.
36. Brekman A, Walters MS, Tilley AE, Crystal RG. FOXJ1 prevents cilia growth inhibition by cigarette smoke in human airway epithelium in vitro. Am J Respir Cell Mol Biol. 2014;51:688–700.
37. Chung M-I, Kwon T, Tu F, Brooks ER, Gupta R, Meyer M, et al. Coordinated genomic control of ciliogenesis and cell movement by RFX2. eLife. 2014;3:e01439.
38. Howes SC, Alushin GM, Shida T, Nachury MV, Nogales E. Effects of tubulin acetylation and tubulin acetyltransferase binding on microtubule structure. Mol Biol Cell. 2014;25:257–66.
39. Frommer A, Hjeij R, Loges NT, Edelbusch C, Jahnke C, Raidt J, et al. Immunofluorescence analysis and diagnosis of primary ciliary dyskinesia with radial spoke defects. Am J Respir Cell Mol Biol. 2015;53:563–73.
40. Bartoloni L, Blouin JL, Pan Y, Gehrig C, Maiti AK, Scamuffa N, et al. Mutations in the DNAH11 (axonemal heavy chain dynein type 11) gene cause one form of situs inversus totalis and most likely primary ciliary dyskinesia. Proc Natl Acad Sci USA. 2002;99:10282–6.
41. Olbrich H, Häffner K, Kispert A, Völkel A, Volz A, Sasmaz G, et al. Mutations in DNAH5 cause primary ciliary dyskinesia and randomization of left-right asymmetry. Nat Genet. 2002;30:143–4.
42. Reilly ML, Benmerah A. Ciliary kinesins beyond IFT: cilium length, disassembly, cargo transport and signalling. Biol Cell. 2019;111:79–94.
43. Horani A, Ferkol TW, Dutcher SK, Brody SL. Genetics and biology of primary ciliary dyskinesia. Paediatr Respir Rev. 2016;18:18–24.
44. Olbrich H, Schmidts M, Werner C, Onoufriadis A, Loges NT, Raidt J, et al. Recessive HYDIN mutations cause primary ciliary dyskinesia without randomization of left-right body asymmetry. Am J Hum Genet. 2012;91:672–84.
45. Cushion TD, Dobyns WB, Mullins JGL, Stoodley N, Chung S-K, Fry AE, et al. Overlapping cortical malformations and mutations in TUBB2B and TUBA1A. Brain. 2013;136:536–48.

46. Tilley AE, Walters MS, Shaykhiev R, Crystal RG. Cilia dysfunction in lung disease. Annu Rev Physiol. 2015;77:379–406.

47. Lobo LJ, Zariwala MA, Noone PG. Primary ciliary dyskinesia. QJM. 2014;107:691–9.

48. Alanin MC, Nielsen KG, von Buchwald C, Skov M, Aanaes K, Høiby N, et al. A longitudinal study of lung bacterial pathogens in patients with primary ciliary dyskinesia. Clin Microbiol Infect. 2015;21:1093.e1091–1097.

49. Gong T, Liu L, Jiang W, Zhou R. DAMP-sensing receptors in sterile inflammation and inflammatory diseases. Nat Rev Immunol. 2020;20:95–112.

50. Ruppert SM, Hawn TR, Arrigoni A, Wight TN, Bollyky PL. Tissue integrity signals communicated by high-molecular weight hyaluronan and the resolution of inflammation. Immunol Res. 2014;58:186–92.

51. Petrey AC, de la Motte CA. Hyaluronan, a crucial regulator of inflammation. Front Immunol. 2014;5:101.

52. Wright SD, Ramos RA, Tobias PS, Ulevitch RJ, Mathison JC. CD14, a receptor for complexes of lipopolysaccharide (LPS) and LPS binding protein. Science. 1990;249:1431–33.

53. Dziarski R, Tapping RI, Tobias PS. Binding of bacterial peptidoglycan to CD14. J Biol Chem. 1998;273:8680–90.

54. Schröder NW, Morath S, Alexander C, Hamann L, Hartung T, Zähringer U, et al. Lipoteichoic acid (LTA) of *Streptococcus pneumoniae* and *Staphylococcus aureus* activates immune cells via Toll-like receptor (TLR)-2, lipopolysaccharide-binding protein (LBP), and CD14, whereas TLR-4 and MD-2 are not involved. J Biol Chem. 2003;278:15587–94.

55. Means TK, Lien E, Yoshimura A, Wang S, Golenbock DT, Fenton MJ. The CD14 ligands lipoarabinomannan and lipopolysaccharide differ in their requirement for Toll-like receptors. J Immunol. 1999;163:6748–55.

56. Miller YI, Viriyakosol S, Binder CJ, Feramisco JR, Kirkland TN, Witztum JL. Minimally modified LDL binds to CD14, induces macrophage spreading via TLR4/MD-2, and inhibits phagocytosis of apoptotic cells. J Biol Chem. 2003;278:1561–8.

57. Taylor KR, Yamasaki K, Radek KA, Di Nardo A, Goodarzi H, Golenbock D, et al. Recognition of hyaluronan released in sterile injury involves a unique receptor complex dependent on Toll-like receptor 4, CD44, and MD-2. J Biol Chem. 2007;282:18265–75.

58. LeBaron RG, Zimmermann DR, Ruoslahti E. Hyaluronate binding properties of versican. J Biol Chem. 1992;267:10003–10.

59. Matsumoto K, Shionyu M, Go M, Shimizu K, Shinomura T, Kimata K, et al. Distinct interaction of versican/PG-M with hyaluronan and link protein. J Biol Chem. 2003;278:41205–12.

60. Kim S, Takahashi H, Lin WW, Descargues P, Grivennikov S, Kim Y, et al. Carcinoma-produced factors activate myeloid cells through TLR2 to stimulate metastasis. Nature. 2009;457:102–6.

61. Hellman U, Karlsson MG, Engström-Laurent A, Cajander S, Dorofte L, Ahlm C, et al. Presence of hyaluronan in lung alveoli in severe Covid-19: an opening for new treatment options? J Biol Chem. 2020;295:15418–22.

62. Xu Z, Shi L, Wang Y, Zhang J, Huang L, Zhang C, et al. Pathological findings of COVID-19 associated with acute respiratory distress syndrome. Lancet Respir Med. 2020;8:420–2.

63. Crosby LM, Waters CM. Epithelial repair mechanisms in the lung. Am J Physiol Lung Cell Mol Physiol. 2010;298:L715–L731.

64. Hubbs AF, Goldsmith WT, Kashon ML, Frazer D, Mercer RR, Battelli LA, et al. Respiratory toxicologic pathology of inhaled diacetyl in sprague-dawley rats. Toxicol Pathol. 2008;36:330–44.

65. Robinot R, Hubert M, de Melo GD, Lazarini F, Bruel T, Smith N, et al. SARS-CoV-2 infection induces the dedifferentiation of multiciliated cells and impairs muco-ciliary clearance. Nat Commun. 2021;12:4354.

66. More SS, Raza A, Vince R. The butter flavorant, diacetyl, forms a covalent adduct with 2-deoxyguanosine, uncoils DNA, and leads to cell death. J Agric Food Chem. 2012;60:3311–7.

67. Chen CJ, Kono H, Golenbock D, Reed G, Akira S, Rock KL. Identification of a key pathway required for the sterile inflammatory response triggered by dying cells. Nat Med. 2007;13:851–6.

68. Fritzsching B, Zhou-Suckow Z, Trojanek JB, Schubert SC, Schatterny J, Hirtz S, et al. Hypoxic epithelial necrosis triggers neutrophilic inflammation via IL-1 receptor signaling in cystic fibrosis lung disease. Am J Respir Crit Care Med. 2015;191:902–13.

69. Iyer SS, Pulskens WP, Sadler JJ, Butter LM, Teske GJ, Ulland TK, et al. Necrotic cells trigger a sterile inflammatory response through the Nlrp3 inflammasome. Proc Natl Acad. Sci. USA. 2009;106:20388–93.

70. Patel MN, Carroll RG, Galván-Peña S, Mills EL, Olden R, Triantafilou M, et al. Inflammasome priming in sterile inflammatory disease. Trends Mol. Med. 2017;23:165–80.

71. Cassel SL, Sutterwala FS. Sterile inflammatory responses mediated by the NLRP3 inflammasome. Eur J Immunol. 2010;40:607–11.

72. Franchi L, Eigenbrod T, Núñez G. Cutting edge: TNF-alpha mediates sensitization to ATP and silica via the NLRP3 inflammasome in the absence of microbial stimulation. J Immunol. 2009;183:792–6.

73. Tanaka T, Narazaki M, Kishimoto T. IL-6 in inflammation, immunity, and disease. Cold Spring Harb Perspect Biol. 2014;6:a016295.

74. Ambalavanan N, Nicola T, Hagood J, Bulger A, Serra R, Murphy-Ullrich J, et al. Transforming growth factor-beta signaling mediates hypoxia-induced pulmonary arterial remodeling and inhibition of alveolar development in newborn mouse lung. Am J Physiol Lung Cell Mol Physiol. 2008;295:L86–L95.

75. Fitzgerald TL, Lertpiriyapong K, Cocco L, Martelli AM, Libra M, Candido S, et al. Roles of EGFR and KRAS and their downstream signaling pathways in pancreatic cancer and pancreatic cancer stem cells. Adv Biol Regul. 2015;59:65–81.

76. Schneider WM, Chevillotte MD, Rice CM. Interferon-stimulated genes: a complex web of host defenses. Annu Rev Immunol. 2014;32:513–45.

77. Kurokawa C, Iankov ID, Galanis E. A key anti-viral protein, RSAD2/VIPERIN, restricts the release of measles virus from infected cells. Virus Res. 2019;263:145–50.

78. Jumat MR, Huong TN, Ravi LI, Stanford R, Tan BH, Sugrue RJ. Viperin protein expression inhibits the late stage of respiratory syncytial virus morphogenesis. Antivir Res. 2015;114:11–20.

79. Tan KS, Olfat F, Phoon MC, Hsu JP, Howe JLC, Seet JE, et al. In vivo and in vitro studies on the antiviral activities of viperin against influenza H1N1 virus infection. J Gen Virol. 2012;93:1269–77.

80. Andrews S. FastQC: a quality control tool for high throughput sequence data. 2010. http://www.bioinformatics.babraham.ac.uk/projects/fastqc/.

81. Krueger F. A wrapper tool around Cutadapt and FastQC to consistently apply quality and adapter trimming to FastQ files, with some extra functionality for MspI-digested RRBS-type (Reduced Representation Bisufite-Seq) libraries. http://www.bioinformatics.babraham.ac.uk/projects/trim_galore/.

82. Kersey PJ, Staines DM, Lawson D, Kulesha E, Derwent P, Humphrey JC, et al. Ensembl genomes: an integrative resource for genome-scale data from non-vertebrate species. Nucleic Acids Res. 2012;40:D91–97.

83. Dobin A, Davis CA, Schlesinger F, Drenkow J, Zaleski C, Jha S, et al. STAR: ultrafast universal RNA-seq aligner. Bioinformatics. 2013;29:15–21.

84. Liao Y, Smyth GK, Shi W. featureCounts: an efficient general purpose program for assigning sequence reads to genomic features. Bioinformatics. 2014;30:923–30.

85. Love MI, Huber W, Anders S. Moderated estimation of fold change and dispersion for RNA-seq data with DESeq2. Genome Biol. 2014;15:550.

86. Huber W, Carey VJ, Gentleman R, Anders S, Carlson M, Carvalho BS, et al. Orchestrating high-throughput genomic analysis with Bioconductor. Nat. Methods. 2015;12:115–21.

87. Zhu A, Ibrahim JG, Love MI. Heavy-tailed prior distributions for sequence count data: removing the noise and preserving large differences. Bioinformatics. 2019;35:2084–92.

AUTHOR CONTRIBUTIONS

SNL, FLK, DMB, SRP, MB, and SMP designed the study and interpreted the data; SNL, FLK, JJT, TT, RG, AEN, DC, and MB performed experiments and analyzed the data; DMB, RG, SRP, MB, and SMP contributed important insights for the interpretation and discussion of the results. SNL drafted the manuscript and SNL and FLK finalized the manuscript. The method used in assigning the authorship order among co-first

authors was decided based on total time contributed to writing the manuscript. All authors read and approved the final manuscript.

COMPETING INTERESTS
SRP provides consulting services to Moderna and Merck and Co Vaccines, unrelated to the content of this manuscript. SMP has received consulting fees from Altavant, Theravance, and BMS and received research funding from AZ, BI, and CareDX, unrelated to the content of this manuscript. The authors have declared that no conflict of interest exists.

ADDITIONAL INFORMATION
Supplementary information The online version contains supplementary material available at https://doi.org/10.1038/s41420-022-00855-3.

Correspondence and requests for materials should be addressed to Maria Blasi.

Reprints and permission information is available at http://www.nature.com/reprints